Int J Adv Manuf Technol (2017) 92:3489–3501
DOI 10.1007/s00170-017-0407-x

ORIGINAL ARTICLE

Numerical modeling and optimization of joint strength in resistance spot welding of galvanized steel sheets

Fatemeh Mirzaei[1] · **Hamid Ghorbani**[1] · **Farhad Kolahan**[1]

Received: 11 September 2016 / Accepted: 5 April 2017 / Published online: 27 April 2017

Abstract Nowadays, the widespread use of resistance spot welding (RSW) in various industries is evidence for the importance of this manufacturing process. In this paper, the finite element method (FEM) is utilized to model the weld nugget geometry and tensile-shear strength in RSW process of the galvanized interstitial free (IF) and bake hardenable (BH) steel sheets. Computational results have good agreement with experimental data. The investigation of input parameters influence, namely welding current, welding time, and electrode force on nugget size variations reveals that welding current is the most influential parameter. The examination of input parameters interaction on joint strength indicates that increase in welding current and time and also reduction in electrode force result in larger nugget size and bigger joint strength. Although by increasing the nugget size, at first, the joint strength is raised, after reaching the maximum strength, increase in nugget size results in decreasing the joint strength, and it may lead to expulsion phenomenon. The analysis of variance (ANOVA) results of response surface methodology (RSM) modeling demonstrate that beside the welding parameters, their interactions have significant effect on nugget geometry and tensile-shear strength. The relative error between RSM predicted and FEM calculated maximum strength is attained about 3% that specifies the efficiency of RSM.

Keywords Resistance spot welding · Finite element analysis · Tensile-shear strength · Optimization · Response surface methodology

1 Introduction

Resistance spot welding (RSW) process is widely used in sheet metal fabrication industries such as automotive and appliances, due to high speed, low cost, and automation capability. This process is carried out in four stages which are squeeze, weld, hold, and off stages. In the first stage, a definite force is exerted to sheets through electrodes so that they are tightly connected to each other. In the welding cycle, in addition to electrode force, electric current is applied to generate heat at the sheets interface and form the weld nugget. In the holding stage, although the current is switched off, the constant electrode force is still employed until the weld nugget can be cooled slowly. Finally, during the off stage, electrodes are lifted from the welded sheets. In this process, weld nugget geometry is the most effective parameter on the mechanical properties of the weld joints especially tensile-shear and fatigue strengths. On the other hand, the nugget geometry is affected by various process parameters such as electrodes geometry, applied force, and welding current and time. Therefore, many experimental and numerical studies have been conducted in order that the effects of welding parameters settings on weld nugget geometry and joints strength are comprehensively investigated.

Eisazadeh et al. [1] and Moshayedi and Sattari-Far [2] studied weld nugget geometry and effect of resistance spot welding process parameters on nugget shape and size using numerical simulation. The numerical results had a good agreement with experimental data. Wang et al. [3] simulated the resistance spot welding process to join dissimilar materials Al-steel with direct couples of the thermal, electrical, and mechanical fields, and also the calculated weld nugget dimensions were verified by empirical results. The weld nugget formation process in resistance spot welding for three sheet assemblies was investigated

---

✉ Fatemeh Mirzaei
fatemehmirzaei_fm@yahoo.com

[1] Department of Mechanical Engineering, Engineering Faculty, Ferdowsi University of Mashhad, Mashhad, Iran

by both experimental measurement and finite element method (FEM) simulation [4, 5]. On the other hand, Shen et al. [6] modeled RSW of three steel sheets with dissimilar material and thickness through numerical method and experimental tests. They showed the stacking sequence of the steel sheets significantly influences the weld nugget size. As mentioned above, in addition to the nugget size, the joint strength is also affected by welding input parameters. Aslanlar et al. [7, 8] empirically showed that increase in welding current and welding time leads to rise in the joint strength. Also, excessive values of welding current and time result in generating more resistance heat and spattering molten metal and consequently decreasing the nugget size and the weld strength [9, 10]. Safari et al. [11] experimentally investigated the effects of welding current, welding time, electrode force, and cooling time on tensile-shear strength and failure mode of resistance spot welds of AISI 201 stainless steel. They showed that the failure mode was changed from pullout mode to pullout with tearing of the sheet mode by increasing the welding current and fusion zone size. Jagadeesha and Jothi [12] determined input parameter values for which the joint strength of spot-welded AISI 316L stainless steel sheets is maximum. Also, they observed three types of breaking failures viz., knotting, tearing, and separation during the tensile-shear tests. Li et al. [13] investigated the weld nugget formation in 5052 aluminum alloy resistance spot welding with three equal thickness sheets and three unequal thickness sheets. The mechanical strength and fracture mode of the weld nuggets at the upper and lower interfaces were also studied using tensile-shear specimen configuration. The welding electrodes shape is another effective factor in evaluating the joints quality of RSW process. Zhang et al. [14] proposed optimized electrodes morphology for obtaining the high joint strength in welding of dissimilar materials. Wang et al. [15] performed the FE modeling to analyze the effects of electrode tip morphology on nugget shape and size. In addition, the failure behaviors were studied through the tensile-shear test considering the influences of electrode tip morphology. Statistical approaches have been employed to optimize the RSW process. Regression modeling of resistance spot welding process of galvanized steel sheets was performed by Luo et al. [16] with design of experiments and analysis of variance. Hamidinejad et al. [17] experimentally modeled the process using the artificial neural network and optimized the tensile-shear strength by genetic algorithm in resistance spot welding of galvanized interstitial free (IF) and bake hardenable (BH) steel sheets. Maalouf and Barsoum [18] presented an alternative method based on nonlinear regression analysis, namely the kernel ridge regression method (KRR) to predict the failure strength of aluminum spot-welded joints as a function of electrode force and welding current and time. Liang et al. [19, 20] simulated weld nugget geometry and tensile-shear strength in sheet to tube resistance spot welding. They predicted the joint strength through mathematical modeling and compared the results with empirical data.

The galvanized IF and BH steel, due to the proper ductility and specific mechanical properties, are widely used in car body manufacturing. In this research, the weld nugget geometry and tensile-shear strength in resistance spot welding of galvanized IF and BH steel sheets is simulated by finite element method. The presented model is validated through experimental tests. Then, the effect of process parameters, namely welding current and time and electrode force on nugget diameter and thickness is investigated. In addition, the process parameters interaction on tensile-shear strength is discussed, and the influence of nugget geometry on the strength variations is explored. Using response surface methodology (RSM), a mathematical model is proposed to determine the weld nugget dimensions and the joint strength in terms of process parameters. Finally, the maximum strength and corresponding welding parameters are predicted utilizing RSM optimization and compared with numerical results.

2 Experimental setup

The resistance spot welding tests were conducted in a single-phase AC 50 Hz equipment by using water-cooled type B (Dome) RWMA electrodes with 7 mm face diameter to join the galvanized interstitial free (IF) and galvanized bake hardenable (BH) steel sheets with 0.67 mm thickness [17]. The chemical composition of the IF and BH steel sheets is given in Tables 1 and 2. Also, the mechanical properties of the investigated steel sheets are shown in Table 3. In order to appear weld nugget and prevent weld splash and spatter, the appropriate ranges of the welding parameters were selected (see Table 4). The tensile-shear tests were carried out at a crosshead of 20 mm/min with a Zwick (Z050) universal testing machine [17]. The dimensions of tensile-shear test specimens were based on ISO 14273, which is illustrated in Fig. 1. After welding process, the samples were prepared for

Table 1 Chemical composition of the IF steel sheets (wt%) [17]

C	Si	S	P	Mn	Ni	Cr
0.003	0.006	0.005	0.018	0.173	0.011	0.031
Mo	V	Cu	Al	Nb	Zn	Ti
0.001	0.002	0.017	0.035	0.001	0.004	0.05

Table 2 Chemical composition of the BH steel sheets (wt%) [17]

C	Si	S	P	Mn	Ni	Cr
0.002	0.005	0.006	0.018	0.162	0.022	0.021
Mo	V	Cu	Al	Nb	Zn	Ti
0.0006	0.001	0.015	0.044	0.005	0.008	0.005

Table 3 Mechanical properties of the IF and BH steel sheets [17]

Material	Yield strength/σ_y (MPa)		Ultimate strength/σ_u (MPa)	
	Before baking	After baking	Before baking	After baking
IF	164.6	164.9	309.8	310.2
BH	186.4	218.1	310.1	310.2

Table 4 Process control parameters and their levels

Parameters	Notations	Units	Level 1	Level 2	Level 3
Welding current	*C*	KA	10	11	12
Electrode force	*F*	Kgf	195	210	225
Welding time	*T*	Cycle (1/50 s)	8	10	12

metallographic examination using standard metallography procedures. The etchant solution of 85 mL H_2O + 15 mL HNO_3 + 5 mL methanol was used for etching and macrography of samples [21]. The macro characteristic parameters of weld joints, namely nugget diameter, nugget thickness, and heat-affected zone (HAZ) width were measured from the metallographic pictures of samples taken on optical microscope. Fig. 2 shows a representative macrostructure of cross-sectioned welded sample with $C = 11$ KA, $T = 10$ cycles, and $F = 210$ Kgf. In addition, the hardness values in the base metal, HAZ, and nugget for samples were measured in Vickers scale with 0.2 Kgf load. The average value of measured hardness in each zone is presented in Table 5. According to this table, weld nugget hardness is more than HAZ and base metal. The strain hardening stemmed from the electrodes force in the holding stage and high cooling rate are main reasons of increasing the weld nugget hardness than other regions.

3 Finite element modeling of RSW process

In the present study, a finite element model is proposed to simulate the nugget geometry and tensile-shear strength of the RSW process. The weld nugget geometry is specified for the purpose that the tensile-shear strength of the weld joint can be analyzed. The flowchart of analysis procedure is shown in Fig. 3. The squeezing cycle is defined as a single load step, and the welding cycle is divided into several load steps. First step includes the mechanical analysis of process in which the force is exerted to the electrodes (squeeze cycle). This step's results include stress field, displacement, deformation, and also contact area and contact pressure changes. This information is the input data for electrical-thermal coupled analysis step. In this stage, by applying the electrical-thermal boundary conditions, the temperature distribution is obtained. These results are used as a nodal thermal load in thermal-mechanical analysis step. The results of this step are contact pressure, contact area, and deformation distributions. These results are sent to the electrical-thermal analysis step in order that contact conditions are changed and generated heat is calculated. This loop is continued until the end of welding time. Coupling time between two analyses at each stage of loading is 0.02 s (one cycle). Finally, the output of the simulation is weld nugget geometry which is determined based on the melting temperature of the sheets.

The main features for simulation of the process including geometry modeling, boundary conditions, and governing equations are thoroughly explained in the next sections.

3.1 Geometric modeling

Since geometry and loading conditions of the sheets and electrodes are axisymmetric, as shown in Fig. 4, a two-dimensional axisymmetric electrical-thermal-mechanical coupled finite element model is employed to simulate the process in commercial software ANSYS 12. In mechanical and thermal-electrical analyses, the 2D axial symmetric elements of Plane42 having four nodes with two degrees of freedom per node, translations in the nodal *X* and *Y* directions (UX, UY), and Plane67 having four nodes with two degrees of freedom per node, temperature and voltage (TEMP, VOLT) are employed respectively. For simulation of 2D surface-to-surface contact at sheet-sheet and sheet-electrode

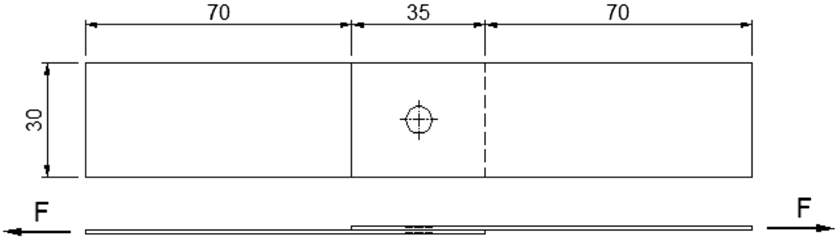

Fig. 1 Dimensions of spot-welded tensile-shear test specimens

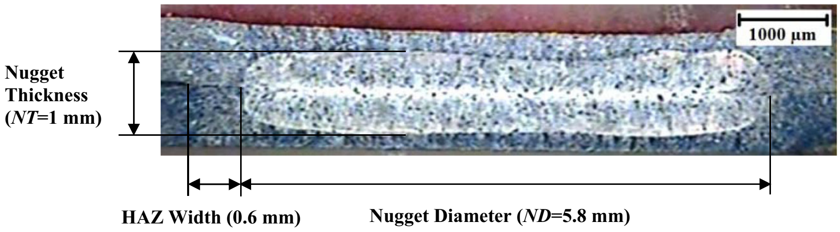

Fig. 2 Macrostructure of cross sectioned welded sample ($C = 11$ KA, $T = 10$ cycles, and $F = 210$ Kgf)

interfaces, the contact pair elements of Conta171 and Targe169 are used. Conta171 element is located on the surfaces of 2D solid elements of Plane42 and Plane67. It has the same geometric characteristics as the solid element face with which it is connected and defined by two nodes with degrees of freedom, UX, UY, TEMP, and VOLT. Targe169 element is used to represent various 2D target surfaces for the associated contact elements of Conta171. Contact occurs when the element surface penetrates (Conta171) one of the target segment elements (Targe169) on a specified target surface. Various properties such as thermal and electric contact conductance, any translational or rotational displacement, temperature, voltage, magnetic potential, forces, and moments can be imposed on the target segment elements to simulate the process. For those parts of the model in which the heat distributions are more important, finer mesh is used, while for other parts, coarse mesh is applied to save computational effort. In total, the model consists of 1214 elements and 1256 nodes.

3.2 Governing equations

The governing equations for electrical, thermal, and mechanical analyses in numerical simulation of process are defined in two-dimensional cylindrical coordinate system. The differential equation for electric field distribution is expressed as follows [22]:

$$\frac{\partial}{\partial r}\left(\mu\frac{\partial\varphi}{\partial r}\right)+\frac{\mu}{r}\frac{\partial\varphi}{\partial r}+\frac{\partial}{\partial z}\left(\mu\frac{\partial\varphi}{\partial z}\right)=0 \tag{1}$$

where r and z are radial and axial coordinates, φ is electrical potential, and μ is electrical conductivity. The governing equation to calculate the heat generated by electrical current according to Joule's law is [22]:

$$Q = RI^2t \tag{2}$$

where Q, I, R, and t are, respectively, heat, electric current, material electrical resistance, and time. Also, Q can be determined using the following equation [22]:

Table 5 Average Vickers hardness measured for different zones in spot-welded joint (kg/mm^2)

Material	Base metal	HAZ	Nugget
Hardness	117	142	198

$$Q=\frac{J_r^2+J_z^2}{\mu} \tag{3}$$

where J_r and J_z are density of passing electrical current along to r and z axes that are defined by Eq. (4) [22]:

$$J_r = -\mu\frac{\partial\varphi}{\partial r} \tag{4a}$$

$$J_z = -\mu\frac{\partial\varphi}{\partial z} \tag{4b}$$

Considering the electrical resistance heat, the governing differential equation for the transient heat transfer problem is obtained as [23]:

$$\rho c\frac{\partial T}{\partial t}=\frac{\partial}{\partial r}\left(k\frac{\partial T}{\partial r}\right)+\frac{k}{r}\frac{\partial T}{\partial r}+\frac{\partial}{\partial z}\left(k\frac{\partial T}{\partial z}\right)+\dot{q} \tag{5}$$

where ρ, c, k, T, and t are density, specific heat, thermal conductivity, temperature, and time, respectively. The term $\dot{q}$ is the rate of the internal heat generation per unit volume within the boundaries of the analysis region. In order to analyze the stress and strain, the governing equation based on thermo-elastic-plastic theory is given by [24]:

$$[d\sigma]=[D^{\mathrm{ep}}][d\varepsilon]-\left[C^{\mathrm{th}}\right]\,dT \tag{6a}$$

$$[D^{\mathrm{ep}}]=[D^{\mathrm{e}}]+[D^{\mathrm{p}}] \tag{6b}$$

where $[D^{\mathrm{ep}}]$, $[D^{\mathrm{e}}]$, and $[D^{\mathrm{p}}]$ are elastic-plastic stiffness matrix, elastic stiffness matrix, and plastic stiffness matrix, respectively. Also, $[d\varepsilon]$, $[d\sigma]$, $[C^{\mathrm{th}}]$, and dT are strain tensor, stress tensor, thermal stiffness matrix, and temperature increment. For structural analysis, the stress equilibrium equation is expressed as [24]:

$$\sigma_{ij}+b_i=0 \tag{7}$$

where b_i is the body force and σ_{ij} is stress tensor.

These equations are solved in software ANSYS to simulate the FE model of RSW process.

3.3 Boundary conditions

The electrical, thermal, and mechanical boundary conditions for the finite element model are shown in Fig. 5.

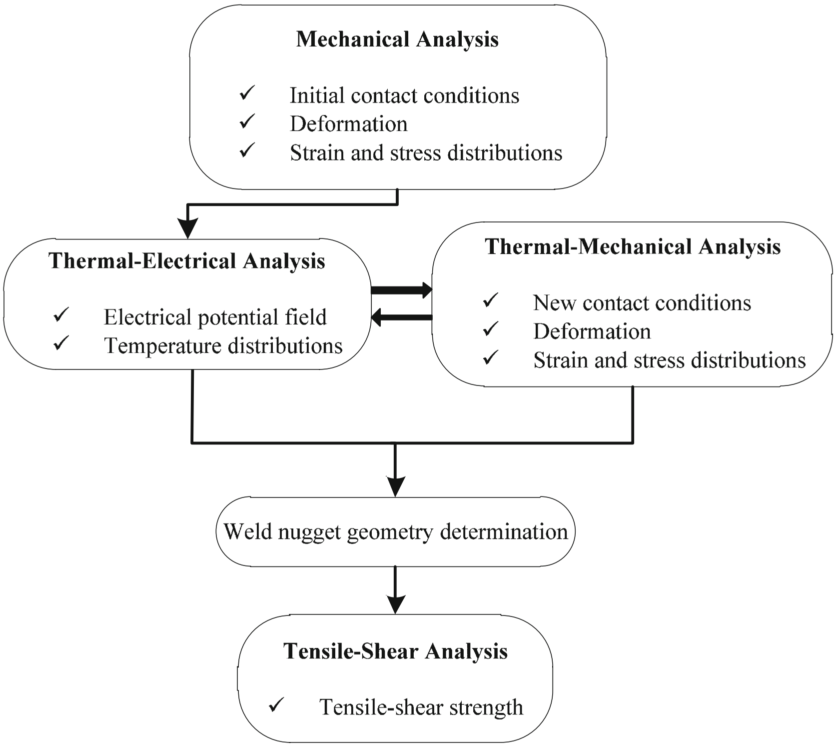

Fig. 3 Modeling procedure flowchart for the finite element analysis of RSW

Because a 50 Hz AC welding machine was used in this research, in the simulation of process, it is assumed that a sine wave electrical current flow with frequency $f = 50$ Hz is uniformly distributed at top surface of upper electrode. Thus, the root-mean-square (rms) value of the welding current is obtained as follows [25]:

$$I_{\rm rms} = \sqrt{\frac{1}{\pi}\int_{0}^{\pi}\left(I_m sin2\pi ft\right)^2 d(2\pi ft)} = \frac{I_m}{\sqrt{2}} \tag{8}$$

where $I_{\rm rms}$ is the rms value, I_m is the peak value, and I is the real value of the welding current. As a result, the welding current which is applied to the model is [25]:

$$I = I_m \sin(2\pi ft) = \sqrt{2}\, I_{rms} \sin(2\pi ft) \tag{9}$$

Electrical potential (V) at bottom surface of lower electrode is set to be zero. The convective heat transfer boundary conditions for lateral surfaces of electrodes

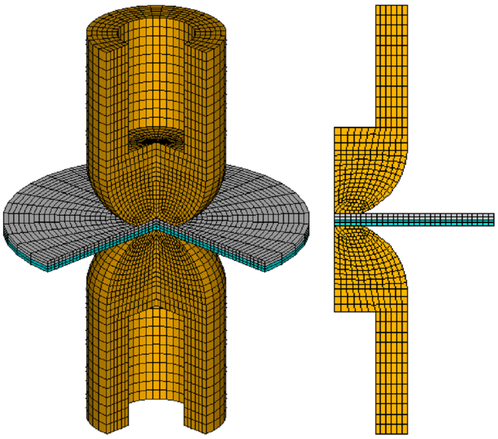

Fig. 4 The finite element model for resistance spot welding

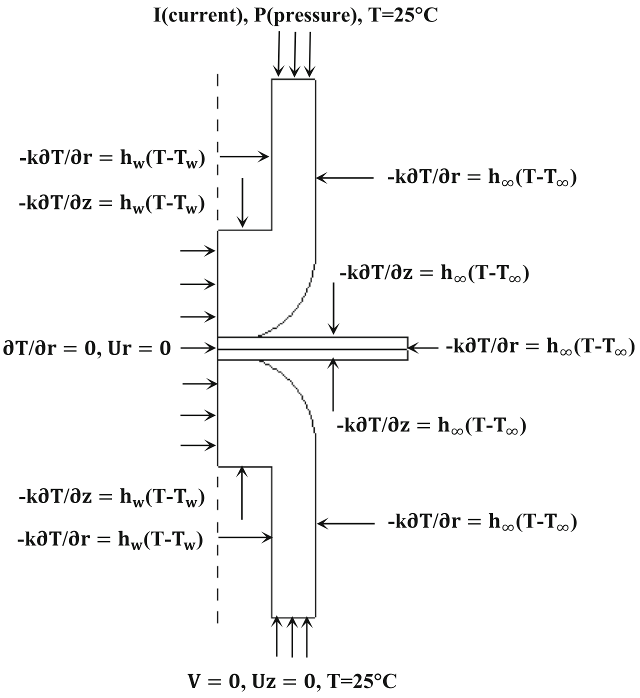

Fig. 5 Schematic of the electrical, thermal, and mechanical boundary conditions

and sheets, which are in contact with ambient air, is given by [23]:

$$q = -k\,\frac{\partial T}{\partial n} = h_\infty (T - T_\infty) \tag{10}$$

Also, the convective heat transfer boundary conditions for inner surfaces of electrodes, which are in contact with water, is [23]:

$$q = -k\,\frac{\partial T}{\partial n} = h_{\mathrm{w}} (T - T_w) \tag{11}$$

where q, h_∞, h_w, T_∞, and T_w are heat generation per unit volume within the boundaries, air convection coefficient 21 kW/m^2, water convection coefficient 300 kW/m^2, air temperature 25 °C, and water temperature 25 °C, respectively. Because of the axial symmetry, half of the geometry is considered to model the electrodes and sheets. Consequently, radiant heat transfer of the central symmetry axis is zero [23]:

$$\frac{\partial T}{\partial r} = 0 \tag{12}$$

Compressive force between the upper and lower electrodes causes the contact of the sheets. For simulation, force applied at top surface of upper electrode increases linearly during the squeeze time and remains constant during the welding and holding times. For bottom surface of lower electrode, there is no force to apply, and axial displacements are restricted. Moreover, radial displacements along the central symmetry axis are also restricted.

The governing equations and boundary conditions are employed in the FE model for simulation of the RSW process in order that the weld nugget geometry and joint strength are calculated.

3.4 Tensile-shear strength analysis

The tensile-shear strength is a main criterion to evaluate the quality of resistance spot-welded joints. Thus, tensile-shear strength of joints is analyzed using weld nugget geometry obtained from simulation results (see Fig. 3). Referring to Fig. 1, during tension test, there is an eccentricity between two tensile axes of the sheets. Therefore, both the tensile and shear stresses play an important role in the joint strength. For mechanical analysis of the welded joint strength, SOLID 45 three-dimensional element is employed. Moreover, it is essential to use different material properties for the nugget, HAZ, and base metal. The mechanical properties of the different regions in spot-welded joint can be seen in Table 6. It is assumed that elasticity modulus (E) and Poisson's ratio (ν) of nugget and HAZ are the same as base metal (E = 200 GPa, ν = 0.3). As shown in Table 3, the yield strength (σ_y) and ultimate tensile strength (σ_u) of the steel sheets are nearly close to each other. Hence, to simplify the analysis, mean values of them are considered as σ_y and σ_u of the base metal $\left(\sigma_{y_{\text{base}}} = 180\ \text{MPa}, \sigma_{u_{\text{base}}} = 310\ \text{MPa}\right)$. Also, to specify mechanical properties of the nugget and HAZ, namely yield and ultimate tensile strengths, hardness values of these regions and base metal should be measured. The average value of measured hardness in each zone under 0.2 Kgf load is presented in Table 5. The scaling ratio k is used to calculate σ_y and σ_u of nugget and HAZ and defined as the ratio of zone hardness (nugget and HAZ) to base metal hardness. According to Table 5, the value of k is obtained 1.7 for nugget and 1.2 for HAZ. Thus, the yield strength and ultimate tensile strength of nugget and HAZ are calculated as follow [20, 26]:

Table 6 Mechanical properties of the different regions in spot-welded joint

Material	Elasticity modulus/E (GPa)	Poisson's ratio/ν	Yield strength/σ_y (MPa)	Ultimate tensile strength/σ_u (MPa)
Base metal	200	0.3	180	310
HAZ	200	0.3	216	346
Nugget	200	0.3	306	436

$$\sigma_y = k.\sigma_{y_{\text{base}}};\quad k = 1.7 \text{ for nugget},\quad k = 1.2 \text{ for HAZ} \tag{13a}$$

$$\sigma_u = \sigma_0 + k.\sigma_{y_{\text{base}}};\, \sigma_0 = \sigma_{u_{\text{base}}} - \sigma_{y_{\text{base}}} \tag{13b}$$

4 Results and discussion

In this section, weld nugget geometry and tensile-shear strength of the spot-welded joints are simulated by FE modeling. Moreover, these results are verified through experimental tests. The welding input parameters effects on nugget size and joint strength are comprehensively investigated. The response surface methodology (RSM) is used to establish a mathematical relationship between inputs and each output of process. Finally, the maximum strength is determined for optimum input parameters using RSM.

4.1 Temperature distribution in spot weld nugget

To verify the weld nugget geometry, the temperature distribution of the weldment is investigated. For instance, the nugget size of the finite element model for input parameters C = 11 KA, T = 10 cycles, and F = 210 Kgf is shown in Fig. 6. The weld nugget is defined as the region in which the temperature is reached above the melting temperature of the sheet material. According to the iron-carbon equilibrium diagram, 1530 °C is considered as the melting point of steel sheets, and region with temperatures higher than 1530 °C is defined as weld nugget displayed in red color.

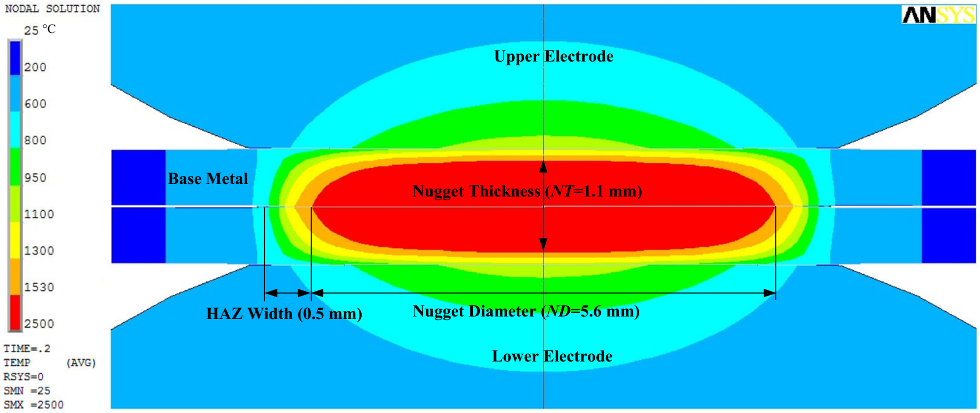

Fig. 6 Temperature distribution (°C) and weld nugget size at the end of welding time ($C = 11$ KA, $T = 10$ cycles, and $F = 210$ Kgf)

Meanwhile, based on this diagram, temperature distribution of the heat-affected zone (HAZ) is almost 750–1530 °C. The results of comparison between simulated and experimental nugget sizes are depicted in Table 7. The relative error between the FE calculated and measured values is 4 to 17%, which indicates a good agreement. Therefore, the finite element modeling is a suitable approach to simulate the weld nugget geometry and analyze the resistance spot welding process accurately.

4.2 Strain and stress distribution in spot weld nugget

The tensile-shear strength as a crucial criterion indicates the quality of joints, so manufacturers try to improve the joint strength in RSW process. In this section, based on the simulated weld nugget geometry, the tensile-shear strength of the spot-welded joint is analyzed. The tensile-shear strength is determined by comparing the maximum Von misses stress with the ultimate tensile strength, in different regions of the base metal, HAZ, and weld nugget. The failure occurs in the region in which the maximum Von misses stress is more than the ultimate stress. Fig. 7a illustrates Von misses stress distribution of the spot-welded sample. The maximum Von misses stress 348 MPa happens in the steel sheet which is greater than its ultimate strength 310 MPa. In other words, the failure occurs in the sheets at the edge of the weld nugget. Also, Von misses strain distribution of the sample is shown in Fig. 7b. It is found that the maximum strain takes place at the same position where failure occurs. The tensile-shear force obtained from simulation and experimental test are 3449.8 and 3698.36 N, respectively. The relative error between numerical and experimental results is less than 7%. This relatively small error indicates that the numerical analysis can accurately predict the joint strength. Hence, FEM simulation can be used as a useful tool with relatively low cost and without destructive tests to investigate the resistance spot welding process and predict its prominent quality measures.

Table 7 Comparison between simulated and experimental nugget size

Geometry	Simulation (mm)	Experimental (mm)	Error %
Nugget diameter	5.6	5.8	3.4
Nugget thickness	1.1	1	10
HAZ width	0.5	0.6	16.6

With regard to the above, the numerical results produced by the developed FE model are used to investigate the concurrent effects of the process parameters settings on the weld nugget geometry and tensile-shear strength. In an attempt to establish a correlation between the two measures, a full factorial design including a total of 27 numerical simulations (three parameters each at three levels listed in Table 4) are conducted.

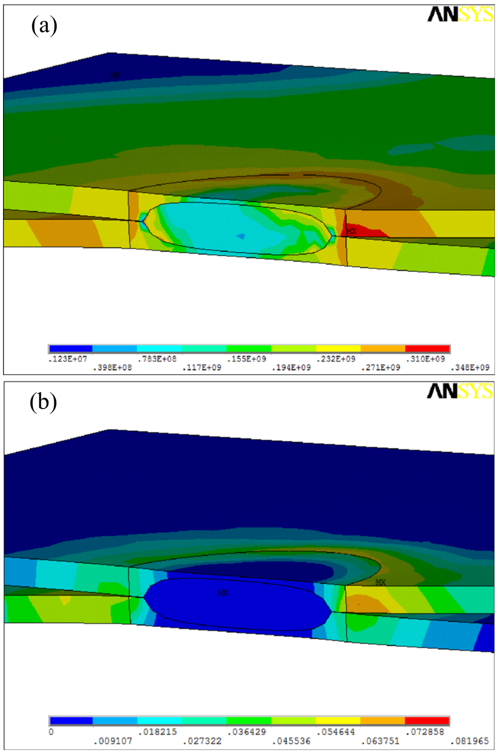

Fig. 7 **a** Von misses stress distribution. **b** Von misses strain distribution in the sample under tensile-shear test ($C = 11$ KA, $T = 10$ cycles, and $F = 210$ Kgf)

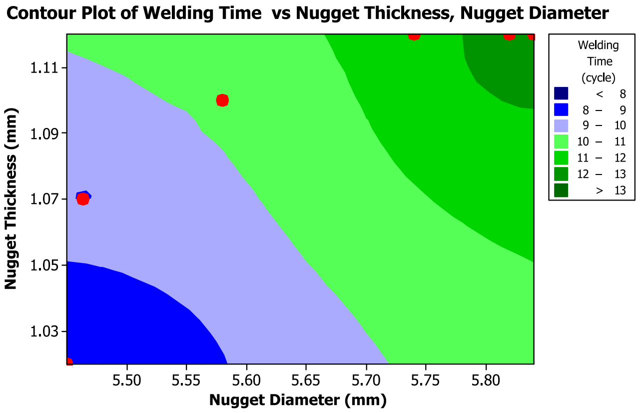

Fig. 8 Effect of welding time on nugget diameter and thickness with 11 KA welding current and 210 Kgf electrode force

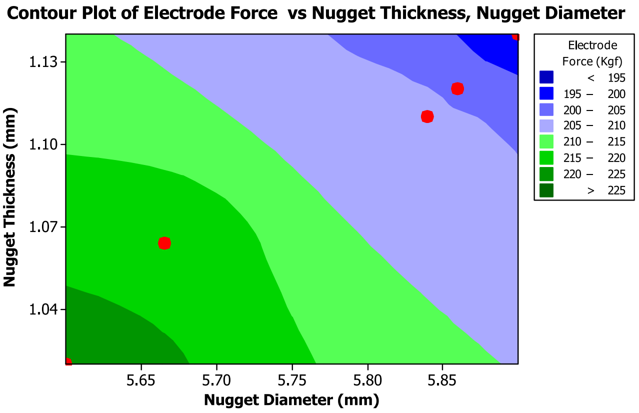

Fig. 10 Effect of electrode force on nugget diameter and thickness with 11 KA welding current and 12 cycles welding time

4.3 Welding parameters effect on the weld nugget geometry

In this section, the effects of welding parameters on weld nugget size are discussed. Figures 8, 9, and 10 show variations in nugget size due to changes in each of the three welding parameters. In each figure, one of the three welding parameters is varied, while the other two are kept constant. Red marks in figures are nugget sizes (diameter, thickness) obtained from numerical simulation of process for certain input welding parameters. These marks are used to clearly illustrate nugget size changes for various input parameters.

For 11 KA welding current and 210 Kgf electrode force, the effect of welding time on nugget diameter and thickness is illustrated in Fig. 8. As expected, increase in welding time causes nugget size to enlarge. However, the rate of nugget size growth decreases, as the welding time becomes longer. In addition, the growth rate of nugget diameter is more than its thickness. It is due to the fact that in longer welding times, the contact area of the faying surface becomes large which causes the current density and contact resistance to reduce. Moreover, by increasing welding time, more heat is lost from fusion zone through conduction and convection.

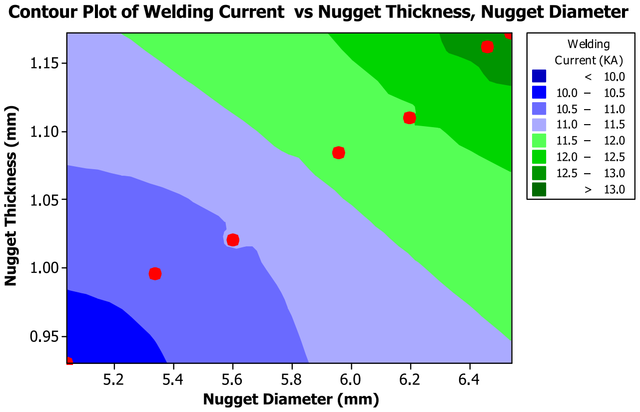

Fig. 9 Effect of welding current on nugget diameter and thickness with 12 cycles welding time and 225 Kgf electrode force

The effect of welding current on nugget diameter and thickness during welding with 12 cycles welding time and 225 Kgf electrode force is shown in Fig. 9. By increasing welding current, both nugget diameter and thickness are constantly raised. This procedure is continued until expulsion phenomenon occurs. According to Figs. 8 and 9, it is seen that the growth rate of weld nugget is more affected by welding current. Hence, increase in welding current is recommended to achieve a proper weld nugget size instead of increase in welding time.

Figure 10 and Table 8 show electrode force influence on nugget diameter and thickness during welding with 11 KA welding current and 12 cycles welding time. According to the figure, the nugget size is reduced when the electrode force is increased. It is due to the fact that increasing the electrode force raises contact area between two sheets, which causes the passing current density to reduce. In addition, high electrode force results in tightly connection between sheets and decrease of the contact resistance. On the other hand, reduction in electrode force to gain greater nugget size leads to expulsion phenomenon. Therefore, selecting a correct electrode force is essential to form a proper weld nugget and achieve the maximum strength.

4.4 Welding parameters interaction on the joint strength

The investigation of welding parameters interaction on the tensile-shear strength of RSW joints is very important in recognition and control of the influential parameters. In this regard, 3D surfaces and their contours are proposed to comprehensively study the interactions. Figures 11, 12, and 13 illustrate the variations in tensile-shear strength when two welding parameters are changed simultaneously and third parameter remains constant. Figure 11 demonstrates welding current and welding time interaction on tensile-shear strength for 225 Kgf electrode force. It can be seen when welding current and time are increased simultaneously, the joint strength is raised. But at higher values of welding current (>11.5 KA)

Table 8 Nugget specifications at different electrode force with 11 KA welding current and 12 cycles welding time

Electrode force (Kgf)	195	225
Nugget center temperature (°C)	2576	2286
2D Contact area (mm)	3.02	3.2
Nugget diameter (mm)	5.9	5.6
Nugget thickness (mm)	1.14	1.02

and welding time (>11 cycles) the strength is reduced. These changes is resulted from the fact that in high values of welding current and time, the excessive resistance heat is generated, and the molten metal is spattered. Besides, in large electrode force, the electrodes penetrate into the sheets and crush them.

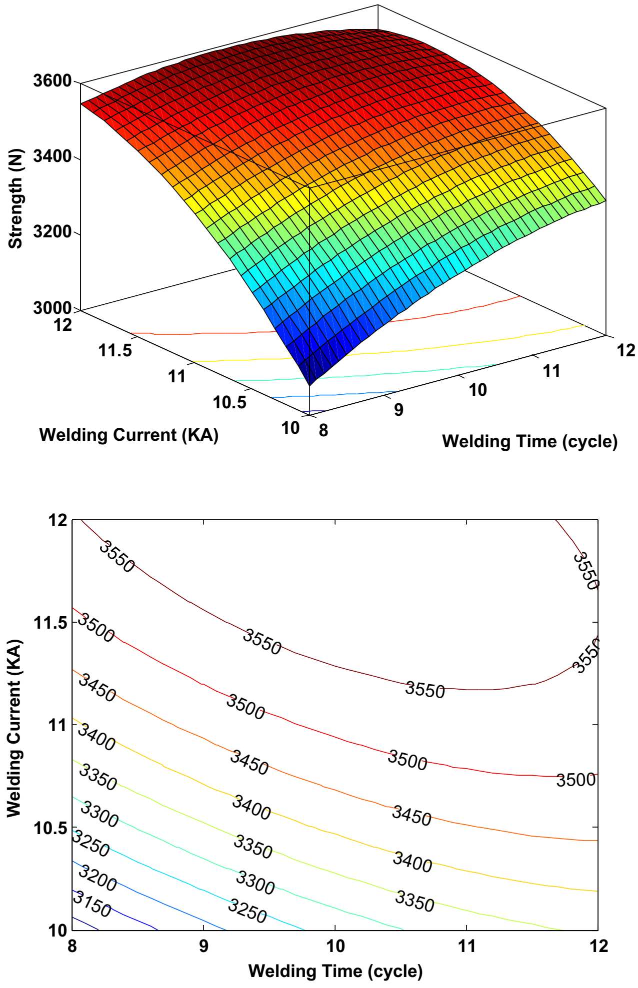

Fig. 11 Welding current and welding time interaction on tensile-shear strength at 225 Kgf electrode force

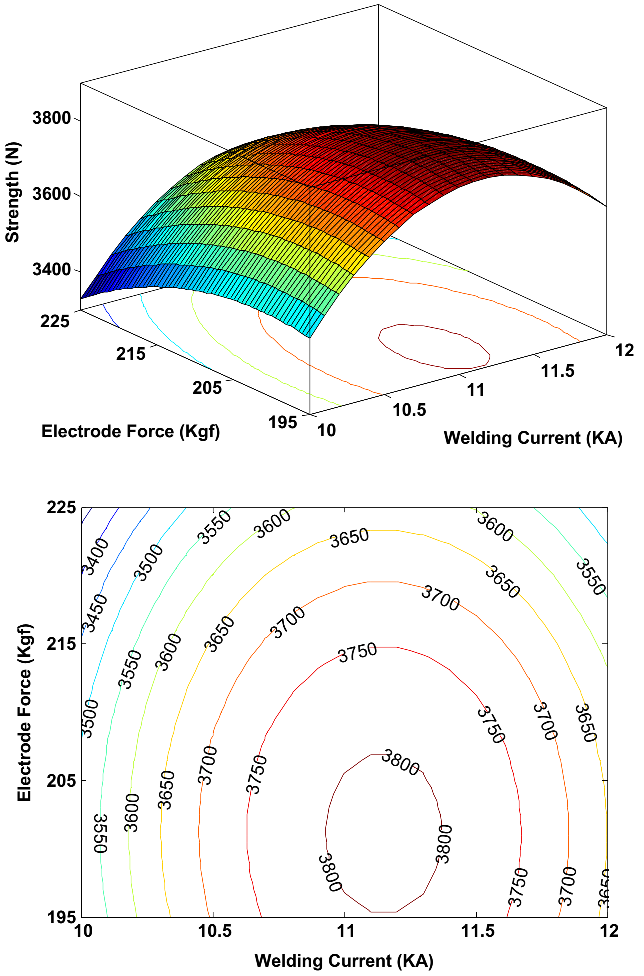

Fig. 12 Welding current and electrode force interaction on tensile-shear strength at 12 cycles welding time

The interaction of welding current and electrode force on tensile-shear strength for 12 cycles welding time is shown in Fig. 12. As can be seen, by increasing welding current and decreasing electrode force simultaneously, the joint strength is increased. This is persisted up to 11 KA welding current and 205 Kgf electrode force, which the strength reaches the maximum amount, and then the strength is declined. As mentioned in Section 4.3, by increasing welding current and decreasing electrode force, nugget size is enlarged, and it leads the joint strength to rise. But at welding currents more than 11 KA and electrode forces less than 205 Kgf, due to the expulsion phenomenon, the strength is reduced. The main reason for this occurrence is that increase in welding current and decrease in contact area under low electrode force result in generating the excessive resistance heat and spattering the molten metal.

The interaction of welding time and electrode force on tensile-shear strength for 12 KA welding current is illustrated in Fig. 13. According to figure, by increasing welding time and decreasing electrode force concurrently, due to raise in nugget size, the joint strength is enlarged. But at higher values of welding time (>10.5 cycles) and lower values of electrode force (<205 Kgf), the joint strength is reduced. The important reason for reducing the strength is the excessive resistance heat generated by the high welding current and low contact area of faying surface.

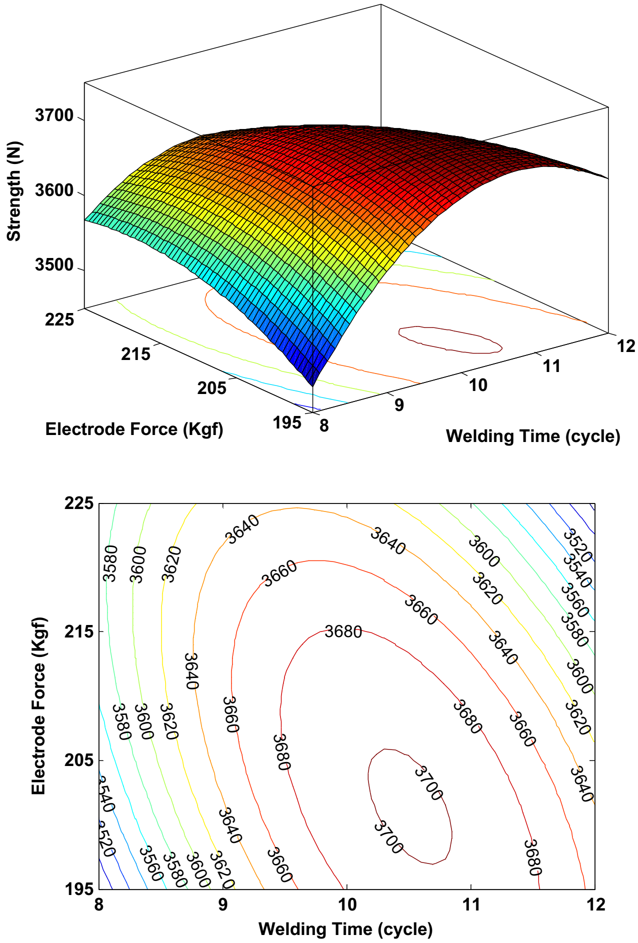

Fig. 13 Welding time and electrode force interaction on tensile-shear strength at 12 KA welding current

4.5 Effect of nugget size on the joint strength

The simultaneous effect of nugget diameter and nugget thickness on tensile-shear strength of the spot-welded joints is depicted in Fig. 14. It can be seen increase in nugget diameter and thickness concurrently, raises the strength to a maximum value; then, the strength is reduced. As mentioned in previous sections, although by increasing welding current and welding time, and decreasing electrode force, the weld nugget size is enlarged, high values of welding current and time result in generating excessive resistance heat, spattering of molten metal, and penetrating electrodes into the sheets.

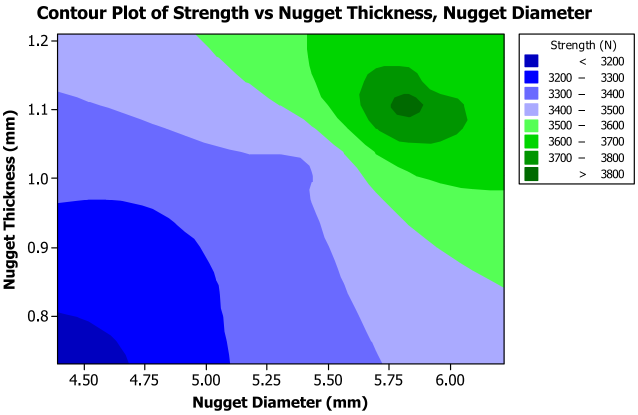

Fig. 14 Effect of nugget diameter and nugget thickness on tensile-shear strength

4.6 Modeling of nugget geometry and strength using RSM

The response surface methodology (RSM) merges both mathematical and statistical techniques for nonlinear modeling of manufacturing processes in which the output variable is influenced by several input variables, and the objective is to optimize the response. The general form of second-order response surface polynomial model is expressed in Eq. (14) [27]:

$$y = b_0 + \sum_{i=1}^{n} b_i x_i + \sum_{i=1}^{n} b_{ii} x_i^2 + \sum_{i<j} \sum b_{ij} x_i x_j + \varepsilon \tag{14}$$

where y is response variable, x_i is a set of independent input variables, b_i is regression coefficients, and ε is residual error. The statistical software Minitab is utilized for mathematical modeling of the process using RSM. The purpose of modeling is to find the suitable functional relationship between the response variables including nugget diameter (ND), nugget thickness (NT), and tensile-shear strength (TS) and welding input parameters (welding current and time and electrode force). The fitted equations of nonlinear RSM modeling for outputs are as follows:

$$\begin{aligned}\mathrm{ND} = {} & -9.55815 + 0.02587\ F + 1.70722\ C + 0.14056\ T - 0.00025\ F^2 - 0.09722\ C^2 - 0.01097\ T^2 \\ & + 0.00494\ FC + 0.00139\ \mathrm{FT} - 0.00917\ CT;\ R\text{–}Sq = 98.59\%\end{aligned} \tag{15}$$

$$\begin{aligned}\mathrm{NT} = {} & -9.28185 + 0.04356\ F + 0.80500\ C + 0.22167T - 0.00012\ F^2 - 0.02778C^2 - 0.00819\ T^2 \\ & + 0.00006\ FC + 0.00036\ \mathrm{FT} - 0.01000\ CT;\ R\text{–}Sq = 98.52\%\end{aligned} \tag{16}$$

$$\begin{aligned}\mathrm{TS} = {} & -18587.0 + 84.3F + 1538.8C + 824.4T - 0.2F^2 - 67.3C^2 - 7.6T^2 + 1.6FC - 1.6\mathrm{FT} - 25.9CT; \\ & R\text{–}Sq = 85.55\%\end{aligned} \tag{17}$$

The analysis of variance is used to check the adequacy of the responses model. In a suitable model, the calculated value of *F*-ratio of ANOVA should be higher than the standard tabulated value of *F*-ratio. Also, the *P*-value is

Table 9 ANOVA for second-order model for *TS*

Source	Degrees of freedom	Sum of squares	Mean squares	$F_{\text{calculated}}$	$F_{0.05}$	*P*-value
Regression	9	701,538	77,948.7	11.18	2.49	0.000
Residual error	17	118,518	6971.6			
Total	26	820,056				

Table 10 ANOVA for model coefficients for *TS*

Source	Degrees of freedom	Sum of squares	Mean squares	$F_{\text{calculated}}$	$F_{0.05}$	*P*-value
F	2	45,795	22,898	8.81	4.46	0.010
C	2	354,285	177,142	68.15	4.46	0.000
T	2	235,463	117,732	45.3	4.46	0.000
$F \times C$	4	8386	2096	0.81	3.84	0.554
$F \times T$	4	37,782	9446	3.63	3.84	0.057
$C \times T$	4	117,551	29,388	11.31	3.84	0.002
Error	8	20,793	2599			
Total	26	820,056				

Table 11 Summary of ANOVA for process outputs

Output	F	C	T	$F \times C$	$F \times T$	$C \times T$
Nugget diameter (ND)	▲	▲	▲	▲		
Nugget thickness (NT)	▲	▲	▲			▲
Tensile-shear strength (TS)	▲	▲	▲		▲	▲

▲ Significant parameters

employed to determine the significance of the model coefficients. If the *P*-value is less or equal to the certain significance level (α-level), the influence of the input variable is significant. In this study, ANOVA for different response variables is carried out with 95% confidence level (*P*-value ≤0.05). For instance, the ANOVA results of the second-order model proposed for tensile-shear strength (TS) given in Eq. (17) is presented in Table 9. According to the table, the *P*-value is less than 0.05 which means the model is significant at 95% confidence level. Also, the calculated *F*-ratio is more than the standard tabulated *F*-ratio, and it means the model is adequate at 95% confidence level. Table 10 represents the ANOVA for individual model coefficients in which welding current and time, electrode force, and the interaction between welding current and time ($C \times T$) have significant effect on TS at 95% confidence level. Moreover, *P*-value for the interaction between electrode force and welding time ($F \times T$) is very close to 0.05; thus, it can be considered a significant factor. Likewise, analysis of variance is performed for ND and NT models given in Eqs. (15) and (16), and summary of results are presented in Table 11. It is obvious that the parameters welding current, welding time, and electrode force have significant effect on all outputs.

4.6.1 Optimization of the joint strength using RSM

Since the maximum tensile-shear strength depends on selection of optimum combination of process parameters, the response surface optimization method is employed to determine the optimum inputs in order that the strength of the spot-welded joints is maximized. The objective function for optimization is set to maximize the strength. The RSM predicted results of input parameters and joint strength are displayed in Table 12. In order to evaluate the accuracy of the strength predicted through RSM, a numerical simulation is carried out based on the predicted input parameters. The calculated maximum strength by FE modeling is 3608.3 N, which corresponds to 6 mm nugget diameter and 1.2 mm nugget thickness. The comparison of predicted and simulated values indicates that the

Table 12 RSM optimization for tensile-shear strength of the spot-welded joint

Electrode force (Kgf)	Welding current (KA)	Welding time (cycle)	Prediction (N)	Simulation (N)	Error %
198	11.4	12	3716	3608.3	3

relative error is about 3%. Thus, the response surface optimization predicts the optimum conditions fairly well.

5 Conclusion

In this paper, the resistance spot welding process of galvanized IF and BH steel sheets is simulated with an electrical-thermal-mechanical coupled finite element model in commercial software ANSYS. Using numerical analysis, nugget geometry and tensile-shear strength of the spot-welded joint under different welding conditions are determined. Due to the good agreement between simulation and experimental results, nugget size and strength of the weld joint can be predicted with computer simulations without costly and time-consuming laboratory research. The results have been enumerated in the following:

1. It was shown that increase in welding time reduces the growth rate of nugget size. Also, the rise of welding current results in increasing the nugget diameter and thickness constantly. This is continued until the expulsion phenomenon occurs. Moreover, by increasing electrode force, the nugget size is reduced because of raise in contact area and decrease in current density and contact resistance.
2. As a result, it is obvious that the nugget size growth rate is more affected by welding current. Hence, in order to achieve proper nugget size, raise in welding current is recommended instead of increase in welding time and decrease in electrode force.
3. It was concluded that by increasing welding current and welding time, and decreasing electrode force, tensile-shear strength is enlarged due to raise in generated heat and nugget size. However, at high welding currents and times, and at low forces, although weld nugget size is increased, the joint strength is reduced.
4. ANOVA results showed that nugget diameter, nugget thickness, and tensile-shear strength are affected by welding current, welding time, and electrode force. The joint strength, in addition to input parameters, is influenced by interaction between welding time and welding current ($T \times C$) and interaction between welding time and electrode force ($T \times F$).
5. Optimization results indicated that the relative error between the maximum strength predicted through RSM and calculated by FEM is about 3%, which proves the precise modeling of process.

This research result can be used to adjust welding parameters and control the nugget size so that the spot-welded joints achieve the maximum strength.

References

1. Eisazadeh H, Hamedi M, Halvaee A (2010) New parametric study of nugget size in resistance spot welding process using finite element method. Mater Des 31(1):149–157
2. Moshayedi H, Sattari-Far I (2012) Numerical and experimental study of nugget size growth in resistance spot welding of austenitic stainless steels. J Mater Process Technol 212(2):347–354
3. Wang J, Wang HP, Lu F, Carlson BE, Sigler DR (2015) Analysis of Al-steel resistance spot welding process by developing a fully coupled multi-physics simulation model. Int J Heat Mass Transf 89:1061–1072
4. Ma N, Murakawa H (2010) Numerical and experimental study on nugget formation in resistance spot welding for three pieces of high strength steel sheets. J Mater Process Technol 210(14):2045–2052
5. Lei Z, Kang H, Liu Y (2011) Finite element analysis for transient thermal characteristics of resistance spot welding process with three sheets assemblies. Procedia Engineering 16:622–631
6. Shen J, Zhang Y, Lai X, Wang PC (2011) Modeling of resistance spot welding of multiple stacks of steel sheets. Mater Des 32(2): 550–560
7. Aslanlar S, Ogur A, Ozsarac U, Ilhan E, Demir Z (2007) Effect of welding current on mechanical properties of galvanized chromided steel sheets in electrical resistance spot welding. Mater Des 28(1):2–7
8. Aslanlar S, Ogur A, Ozsarac U, Ilhan E (2008) Welding time effect on mechanical properties of automotive sheets in electrical resistance spot welding. Mater Des 29(7):1427–1431
9. Martin O, De Tiedra P, Lopez M, San-Juan M, Garcia C, Martin F, Blanco Y (2009) Quality prediction of resistance spot welding joints of 304 austenitic stainless steel. Mater Des 30(1):68–77
10. Pereira AM, Ferreira JM, Loureiro A, Costa JDM, Bartolo PJ (2010) Effect of process parameters on the strength of resistance spot welds in 6082-T6 aluminium alloy. Mater Des 31(5):2454–2463
11. Safari M, Mostaan H, Yadegari Kh H, Asgari D(2016) Effects of process parameters on tensile-shear strength and failure mode of resistance spot welds of AISI 201 stainless steel. The International Journal of Advanced Manufacturing Technology; 1–11.
12. Jagadeesha T, Jothi TJS (2015) Studies on the influence of process parameters on the AISI 316L resistance spot-welded specimens. The International Journal of Advanced Manufacturing Technology ; 1–16.
13. Li Y, Yan F, Luo Z, Chao YJ, Ao S, Cui X (2015) Weld growth mechanisms and failure behavior of three-sheet resistance spot welds made of 5052 aluminum alloy. J Mater Eng Perform 24(6): 2546–2555
14. Zhang W, Sun D, Han L, Li Y (2015) Optimised design of electrode morphology for novel dissimilar resistance spot welding of aluminium alloy and galvanised high strength steel. Mater Des 85:461–470
15. Wang B, Hua L, Wang X, Song Y, Liu Y (2016) Effects of electrode tip morphology on resistance spot welding quality of DP590 dual-phase steel. Int J Adv Manuf Technol 83(9–12):1917–1926
16. Luo Y, Liu J, Xu H, Xiong C, Liu L (2009) Regression modeling and process analysis of resistance spot welding on galvanized steel sheet. Mater Des 30(7):2547–2555
17. Hamidinejad SM, Kolahan F, Kokabi AH (2012) The modeling and process analysis of resistance spot welding on galvanized steel sheets used in car body manufacturing. Mater Des 34:759–767
18. Maalouf M, Barsoum Z (2017) Failure strength prediction of aluminum spot-welded joints using kernel ridge regression. The International Journal of Advanced Manufacturing Technology; 1–9.
19. Liang CP, Lin ZQ, Chen GL, Li YB (2006) Numerical analysis of single sided spot welding process used in sheet to tube joining. Sci Technol Weld Join 11(5):609–617
20. Liang C, Liu X (2009) Strength prediction of sheet to tube single sided resistance spot welding. Mater Des 30(10):4328–4334

21. ASM Metals Handbook, Metallography and microstructures, Vol. 9, 2004
22. Kraus AD, Bar-Cohen A (1983) Thermal analysis and control of electronic equipment. McGraw-Hill, New York
23. Incropera FP, DeWitt DP (1990) Introduction to heat transfer, 2nd edn. John Wiley & Sons, New York
24. Timoshenko SP, Goodier JN (1970) Theory of elasticity, 3rd edn. McGraw-Hill, New York
25. Li YB, Lin ZQ, Hu SJ, Chen GL (2007) Numerical analysis of magnetic fluid dynamics behaviors during resistance spot welding. J Appl Phys 101(5):053506
26. Zhou M, Hu SJ, Zhang H (1999) Critical specimen sizes for tensile-shear testing of steel sheets. Weld J 78:305s–313s
27. Montgomery DC (2001) Design and analysis of experiments. Wiley, New York